

Constant Transmembrane Pressure vs. Constant Permeate Flux: Effect of Particle Size on Crossflow Membrane Filtration

Volodymyr V. Tarabara,¹ Rik M. Hovinga,² and Mark R. Wiesner^{1,*}

¹*Environmental and Energy Systems Institute*

²*Department of Civil and Environmental Engineering
Rice University
Houston, TX 77005-1892*

ABSTRACT

A series of membrane filtration experiments was carried out in a crossflow flat slit geometry to study permeate flux dependence on particle size and operational mode. Dilute monodisperse suspensions of polystyrene particles 20, 50, 100, and 680 nm in diameter were filtered in both constant permeate flux (CF) and constant transmembrane pressure (CP) crossflow regimes using laboratory membrane cell with a known flow configuration. In addition to particle size, other controlled parameters included temperature, crossflow velocity, bulk suspension concentration, transmembrane pressure, membrane hydraulic resistance, and surface chemistry of particles and the membrane. Obtained experimental specific permeate flux profiles were used to evaluate the transient permeate flux model by Sethi and Wiesner. The extended model was found to significantly overpredict permeate flux for medium-size particles (50–100 nm) while providing reasonable agreement with experimental data for small (20 nm) and big (680 nm) particles. Despite these discrepancies, experimentally observed differences between performance in CP and CF modes were in good qualitative agreement with model predictions. The CP operation mode yielded higher specific permeate flux, with the difference decreasing as particle size increased. Further, the extended model was modified to allow for parametric studies of permeate flux using descriptors of the cake morphology as fitting parameters. It was shown that changes in cake morphology alone could not account for the discrepancies observed for medium-sized particles. These results suggest additional back-transport mechanism(s) not currently included in the model. Preferential resuspension and scouring of medium-sized particles were hypothesized as such mechanisms.

Key words: microfiltration; ultrafiltration; fouling; permeate flux; cake morphology

*Corresponding author: Environmental and Energy Systems Institute, Rice University, MS 316, P.O. Box 1892, Houston, TX 77005. Phone: 713-348-5129; Fax: 713-348-5203; E-mail: wiesner@rice.edu

INTRODUCTION

CROSSFLOW MEMBRANE FILTRATION may be performed under conditions of either constant transmembrane pressure or constant flux. In contrast with dead-end filtration, the feed stream is directed tangentially to the membrane surface and a portion of “concentrate” remains in the module while the rest of the fluid exits as permeate. The goal of the tangential flow is to arrest the growth of the fouling layer and thereby retain a higher permeate flux. The more complex hydrodynamics of a crossflow filtration module entail a suite of particle transport mechanisms that are sensitive to the type of suspension to be filtered. In this work, we consider the role of particle size as it may differentially influence membrane fouling in constant transmembrane pressure or constant permeate flux operation.

A considerable amount of research effort has been directed towards better understanding membrane fouling by particular materials. Particles may deposit on the membrane surface forming a cake that may reduce membrane permeability. Investigations of particle transport and fouling in membrane filtration have typically focused on single mechanisms including inertial lift (Green and Belfort, 1980), Brownian diffusion (Blatt *et al.*, 1970; Porter, 1972), shear-induced diffusion (Zydney and Colton, 1986; Davis and Leighton, 1987; Davis and Sherwood, 1990; Romero and Davis, 1990), surface transport (Stamatikis and Tien, 1993), and concentrated flowing layers (Leonard and Vasilieff, 1984). The detailed account of the work in this area may be found in several reviews on the subject (Belfort *et al.*, 1994; Bowen and Jenner, 1995; Wiesner and Chellam, 1999; Ripperger and Altmann, 2002).

Sethi and Wiesner (1997) extended the shear-induced diffusivity model of Romero and Davis (1990) to con-

sider Brownian diffusion and inertial lift as well as shear-induced diffusivity and concentrated flowing layers as the transport mechanisms in a transient model of crossflow filtration (Fig. 1). This extended model is briefly summarized here.

Hydraulic cake resistance R_c is estimated using Carman-Kozeny correlation (1) and related to permeate flux by Darcy's law (2):

$$R_c = R_c^* \delta_c = \frac{45 \varphi_c^2}{a_p^2 (1 - \varphi_c)^3} \delta_c \quad (1)$$

where a_p is the particle radius, φ_c is the solidosity of the cake taken to be equal to 0.58 (corresponding to the random packing density), δ_c is the cake thickness, R_c^* is the specific cake resistance, and the permeate flux is calculated as

$$J = \frac{\Delta P}{\mu_o(R_m + R_c)} = \frac{J_m}{(1 + R_c/R_m)} \quad (2)$$

where ΔP is the transmembrane pressure, R_m is the membrane resistance, R_c is the cake resistance, and $J_m = \Delta P/\mu_o R_m$ is the water flux through the unfouled membrane.

To formulate the model, equations expressing microscopic momentum balance and particle mass balance are employed. The axes x and y are in the direction along and normal to the membrane respectively, while u and v are velocity in x and y directions. Derivation of microscopic momentum balance (3) involves the following assumptions: (a) the particle flowing layer is thin, so that shear stress can be taken as constant; (b) suspension flow is fully developed and in steady state; (c) permeate velocity is much smaller than crossflow velocity so that concentration and velocity profiles change only slowly with x ; and (d) viscosity is concentration dependent but the suspension still behaves as a Newtonian fluid. Under

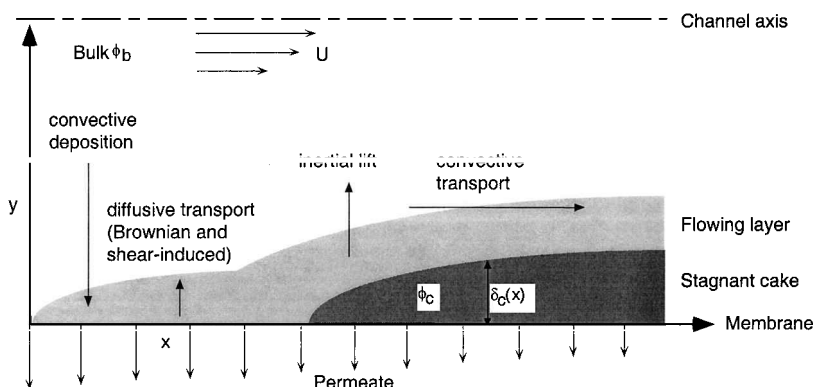


Figure 1. Approach to mass transfer and schematic of flowing and cake layers. Adapted in modified form from Romero and Davis (1990).

the latter assumption the local shear rate can be expressed as

$$\dot{\gamma} = \left| \frac{du}{dy} \right| = \frac{\tau_w}{\mu_o \mu(\varphi)} \quad (3)$$

where τ_w is the wall shear stress and $\mu(\varphi)$ is the relative viscosity, estimated from Leighton's experimental correlation (Leighton and Acrivos, 1987):

$$\mu(\varphi) = \left(1 + \frac{1.5\varphi}{1 - \varphi/\varphi_c} \right)^2.$$

A reduced form of the convective diffusion Equation (4) expressing microscopic particle mass balance is obtained and further simplified by omitting the axial diffusion term, and the term $-\partial(\mu\varphi)/(\partial x)$ describing axial convection (Romero and Davis, 1990) because it is small relative to lateral convection term.

$$-\frac{\partial(u\varphi)}{\partial x} - \frac{\partial(v\varphi)}{\partial y} + \frac{\partial}{\partial y} \left(D \frac{\partial\varphi}{\partial y} \right) = \frac{\partial\varphi}{\partial t} \quad (4)$$

The transient term $(\partial\varphi)/\partial t$ is also omitted because it relates to other terms in (4) as (bulk suspension volume fraction)/(average volume fraction within the flowing layer) $\ll 1$. Thus, (4) can be reduced to

$$[D_b + D_s(\varphi)] \frac{d\varphi}{dy} + v_w \varphi = 0 \quad (5)$$

Integrating (5) across the entire cake layer results in a partial differential equation describing the net transport of particles towards the membrane. After substituting the expression for local velocity determined from (3) into this

equation and performing nondimensionalization, the following expression for the particle flux balance is obtained:

$$g(\hat{\delta}) \frac{\partial \hat{\delta}}{\partial \hat{t}} + h(\hat{\delta}) \frac{\partial \hat{\delta}}{\partial \hat{x}} = f(\hat{\delta}) \quad (6)$$

where $\hat{\delta}$ is the nondimensional cake thickness, and g , h , and f are complex functions of $\hat{\delta}$ (Sethi and Wiesner, 1997). To solve (6), Sethi and Wiesner employed the MacCormack method based on a predictor-corrector methodology.

The extended model predicted that for particles of intermediate size (~ 100 nm) the relative cake buildup is maximized due to a net minimum in back-transport mechanisms superimposed on the effect of increasing specific cake resistance with decreasing particle size.

Both CP and CF modes of operation were modeled. Modeling of CF regime was based on updating the value of the transmembrane pressure thereby decomposing the model of CF operation into a sequence of short CP operations. Simulations comparing CF and CP modes of operation (Fig. 2) suggested increasing benefits of the CP mode as particle size decreases.

In this article, we examine effects of particle size and mode of operation on the transient behavior of permeate flux and compare them with predictions of the extended model. We also describe a modification to the extended model, which incorporates the possibility of varying the morphology of the cake. Two additional parameters describing the cake surface—cake solid fraction at the wall, and thickness of the transition zone—are introduced. The

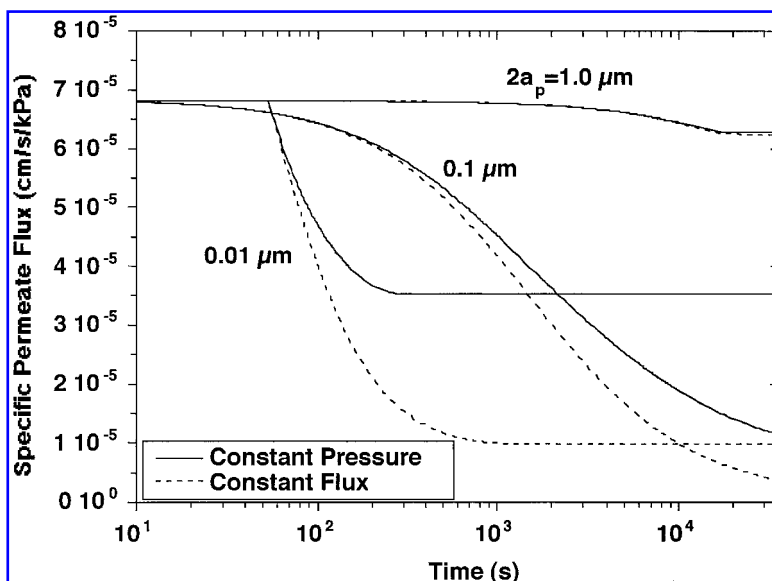


Figure 2. Comparison between constant pressure and constant flux modes of operation for different particle sizes from Sethi and Wiesner (1997).

dependence of permeate flux behavior on the values of these two parameters is presented.

MATERIALS AND METHODS

Membrane filtration setup

The ultrafiltration membrane setup (Fig. 3) was constructed based on the medium/high foulant configuration of SEPA acrylic crossflow flat slit membrane filtration cell (SEPA CF, Osmonics, Minnetonka, MN) able to withstand pressures up to 100 psi (~ 690 kPa). The trans-membrane pressure was regulated by a pressurized air cylinder and read from a pressure gauge (E.N.F.M. B.V., Schiedam, The Netherlands; 0–100 PSI) attached to the cell body. A 7.4-liters capacity aluminum feed tank was custom built to withstand an internal pressure over 1,750 kPa. Tubing used for the feed cycle and permeate cycle consisted of 1/4" and 3/8" outer diameter Teflon FEP

tubes (Cole Parmer, Chicago, IL; 06406-66 and 06406-74).

The feed suspension was pumped over the membrane in a recycle loop by a pulse-free centrifugal pump (EC-J1, Pulsafeeder, Rochester, NY). Stirring at the rate of 6 L/min was provided by the bypass loop. A stainless steel needle valve was used to control the feed flow that had a range of 0–3 L/min.

The temperature was kept constant at $20.0^\circ \pm 0.1^\circ\text{C}$ by recirculating methanol through a cooling loop consisting of a chiller (KR30A, PolyScience, Niles, IL), a pump (3-MDX, Little Giant Pump Co., Oklahoma City, OK), a thermosensor, and a temperature control unit (DynaSense, Model No. 2158, Cole Parmer). For the cooling cycle, 3/8" inner diameter Tygon tubing (Cole Parmer; 06408-12) was used outside the feedtank and 3/8" outer diameter stainless steel tubing (Cole Parmer; 03300-15) was used inside the feedtank.

An on-line spectrophotometer (Spectra 100, Spectra-

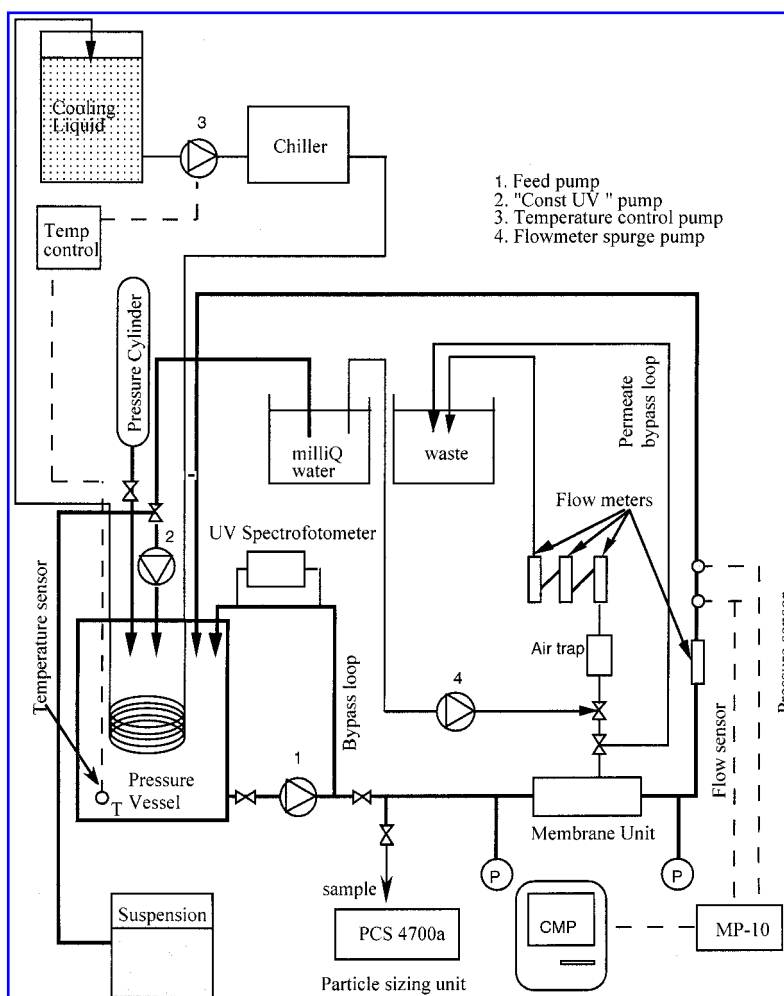


Figure 3. Flow chart of the setup.

Physics, San Jose, CA) equipped with a flow-through cell (path length 3 mm) was used to control bulk concentration of particles in the suspension. Absorption by the feed suspension at $\lambda = 245$ nm was recorded in real time, and the suspension concentration was kept constant by pumping either pure water (positive displacement diaphragm pump, LMI, Acton, MA; B111-391SI), or the concentrated particle suspension (positive displacement diaphragm pump, LMI, Acton, MA; A141-155) into the feed tank. In addition, photon-correlation spectroscopy (PCS) was used to monitor aggregation state of the suspension by measuring particle size distribution of feed suspension samples.

Digital flow meters were found to provide unreliable readings for small flows such as those involved in our experiments. Instead, flow rate was measured using calibrated variable area flow meters with a glass float. In the course of experiments, air had a tendency to dissolve into the water on the feed side of the membrane, which lead to air bubbles forming in the tubing and inside flowmeters on the permeate side. If these bubbles attached themselves to the glass balls inside the flowmeters, an incorrect reading resulted. To avoid this problem an air trap was installed. In addition, to eliminate bubbles, flowmeters were sparged using another pump (Masterflex, Model No. 07553-20, Cole Parmer). The initial permeate flow rate was $149 \text{ L/m}^2/\text{h}$, which corresponds to the permeate velocity of $4.15 \cdot 10^{-3} \text{ cm/s}$ for a membrane area of 21.28 cm^2 . The crossflow velocity was kept constant at 11.6 cm/s value.

Membrane filtration cell and membranes

The flow region of the SEPA CF cell used in our experiments may be decomposed into five subregions (Fig. 4): inlet and outlet tubes, narrow flat slit (channel) di-

recting the flow normal to the axes of inlet and outlet tubes, and two cylindrical ducts connecting inlet and outlet tubes with the channel. The cell used in our experiments was reconfigured so that the membrane was pressed against the lower wall of the channel. Thus, after entering the cell through the inlet tube, the flow turns 90 degrees, enters the channel, passes over the membrane, makes another 90-degree turn to enter the outlet tube, and exits the system. The length, the width, and the height of the channel are 148, 96, and 1.73 mm, correspondingly. After taking into the account the rounding of channel's corners, these dimensions translate to a membrane area of 14051.27 mm^2 and a cross-sectional flow area of 166.08 mm^2 .

Examination of a membrane fouled by $1\text{-}\mu\text{m}$ particles in preliminary filtration experiments revealed an inhomogeneous deposition pattern due to the fact that the flow is not unidirectional over the entire membrane area. Computational fluid dynamics modeling of the flow within a crossflow membrane filtration cell with dimensions replicating those of the SEPA CF cell was performed to determine a location within the cell where the flow could be considered unidirectional (Tarabara and Wiesner, 2002). The flow was found to be largely unidirectional over most of the channel area with the exception of the corners of the channel. To isolate peripheral areas of the membrane from the crossflow, adhesive tape was applied to the permeate side of the membrane rendering the effective area of membrane to be 21.28 cm^2 .

All experiments were performed using polysulphone membranes chemically modified to have a hydrophilic surface (NTR-7410, Hydranautics, Oceanside, CA). Membranes with a molecular weight cutoff of 7,000 Daltons (roughly equivalent to a pore diameter of $\sim 2 \text{ nm}$), were chosen to eliminate the possibility of pore plugging. The sample membrane sheet of 1 m^2 area was cut into

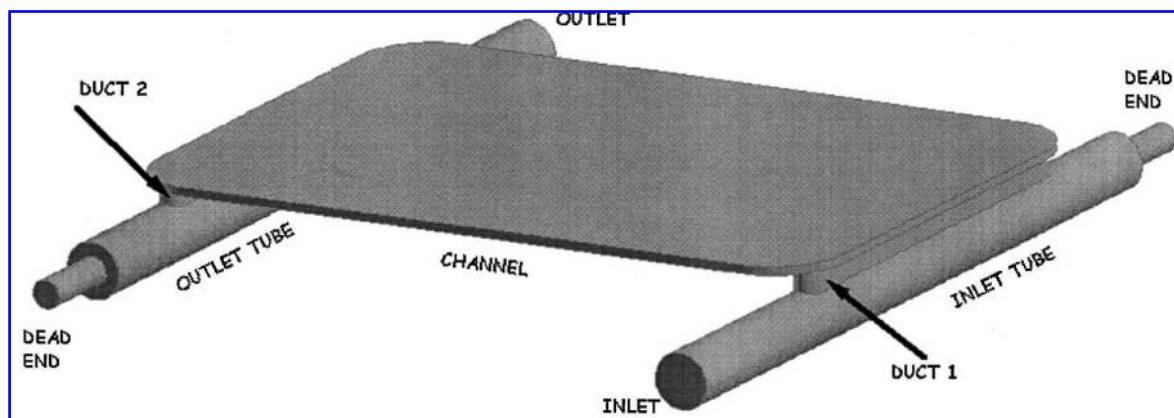


Figure 4. Geometry of the SEPA CF cell.

smaller pieces of the appropriate size (19×14 cm, with rounded corners) to fit the SEPA CF cell.

Clean water flux tests were performed for all membranes used in all experiments. The tests provided information on the integrity of the system ensuring that there were no tears or other imperfections on the membrane surface. As determined by clean water flux tests, the average resistance of this membrane was $(1.08 \pm 0.22) \cdot 10^{-10} \text{ cm}^{-1}$. To ensure analogous fouling conditions for all membranes, the initial transmembrane pressure was adjusted to yield the same initial permeate flux for all experiments.

After performing a clean water flux test, each membrane was compressed at 621 kPa transmembrane pressure until the clean water flux stabilized before filtration experiment. The time of compression varied for different membrane samples and was in the range of 30–90 min.

At the end of each experiment, the feed suspension was discarded, Millipore water was introduced into the feed tank, and a final clean water flux test was run. Membrane was removed from the filtration cell and cake was visually inspected. To store fouled membranes, 0.05% solution of NaN_3 was used to inhibit bacterial growth.

Particles

Spherical polystyrene particles (Bangs Laboratories Inc., Fishers, IN) of four different sizes were used in our experiments: 20, 50, 100, and 680 nm. Particles were suspended in ultrapure water (Milli-Q system, Millipore Corporation, Bedford, MA) with electrical conductivity of $0.49 \pm 0.01 \mu\text{S/cm}$. pH varied in the range from 6.3 to 6.6, with the average of 6.4 and the standard deviation of 0.2. The solid fraction (volume/volume) of particles was 10^{-4} for all particle sizes. After particles were suspended, the electrical conductivity of the solution was measured again and found to be equal to 0.92 ± 0.02 , 2.44 ± 0.02 , 0.89 ± 0.01 , and $0.92 \pm 0.02 \mu\text{S/cm}$ for 20, 50, 100, and 680 nm particles, correspondingly. For the 50-nm particles, another conductivity measurement was performed for particles from another lot (same size, shipped separately by the manufacturer) and a result similar to the first measurement for particles of this size was obtained ($2.55 \pm 0.04 \mu\text{S/cm}$). All measurements were carried out using M90 conductivity meter (Corning Inc., Corning, NY). All values of standard deviations indicated above correspond to the 95% confidence interval. Using the following relationship between ionic strength and electrical conductivity (Standard Methods, 1980):

$$IS = 1.6 \cdot 10^{-5} EC \left(\frac{\mu\text{S}}{\text{cm}} \right) \quad (7)$$

the ionic strength was estimated to be $1.5 \cdot 10^{-5}$, $3.9 \cdot 10^{-5}$, $1.4 \cdot 10^{-5}$, and $1.5 \cdot 10^{-5}$ for suspensions of 20-, 50-, 100-, and 680-nm particles, correspondingly. Suspensions were not buffered to keep the ionic strength low.

Manufacture-supplied data on the particle size distribution of these suspensions were verified using PCS and SEM analyses. PCS tests (PCS 4700a, Malvern Instruments, Malvern, UK) were performed using 10-mm round cells for multiangle sizing (PCS8400, Malvern Instruments). SEM images were recorded using Philips XL-30 FEG environmental scanning electron microscope.

Samples of suspension were taken periodically from the filtration module in the course of filtration experiments to measure the particle size distribution. Aggregation was undetectable in all of the experiments.

RESULTS AND DISCUSSION

A total of 19 crossflow membrane filtration experiments with monodisperse suspensions of polystyrene particles of four different sizes were carried out in CF and CP regimes (Tables 1 and 2). Initially, to verify the predicted dependence of the transient and steady-state permeate flux on the particle size, polystyrene particles 20, 100, and 680 nm in diameter were chosen. However, preliminary results indicated distinctly different dynamics of

Table 1. Summary of experimental conditions.

Exp. no.	Type of exp.	Particle size, nm	Membrane resistance, $\cdot 10^{-10}, \text{cm}^{-1}$	UV absorption (at 250 nm)
1	CP	20	1.33	0.011
2	CP	20	1.43	n/a
3	CP	20	0.97	0.011
4	CF	20	0.93	n/a
5	CF	20	n/a	n/a
6	CP	50	1.26	0.445
7	CP	50	1.16	0.300
8	CF	50	0.76	0.448
9	CF	50	1.13	0.443
10	CP	116	1.09	0.959
11	CP	116	1.19	0.963
12	CP	100	1.04	0.968
13	CF	100	0.89	0.965
14	CF	100	0.85	0.967
15	CP	680	1.55	0.406
16	CP	680	1.27	0.396
17	CP	650	0.89	0.468
18	CF	670	0.92	0.405
19	CF	670	0.84	0.406

Table 2. Values of operational parameters used in filtration experiments.

Parameter	For 20 nm particles	For 50 nm particles	For 100 nm particles	For 680 nm particles
Average transmembrane pressure, ^a kPa	473	455	485	450
Bulk suspension volume fraction		0.001		
Initial permeate flux, mL/min		5.33		
Average crossflow velocity at inlet, cm/s		11.6		
Membrane length, cm		2.3		
Average membrane resistance, ^a $\cdot 10^{-10}$, cm^{-1}	1.24	1.21	1.11	1.24

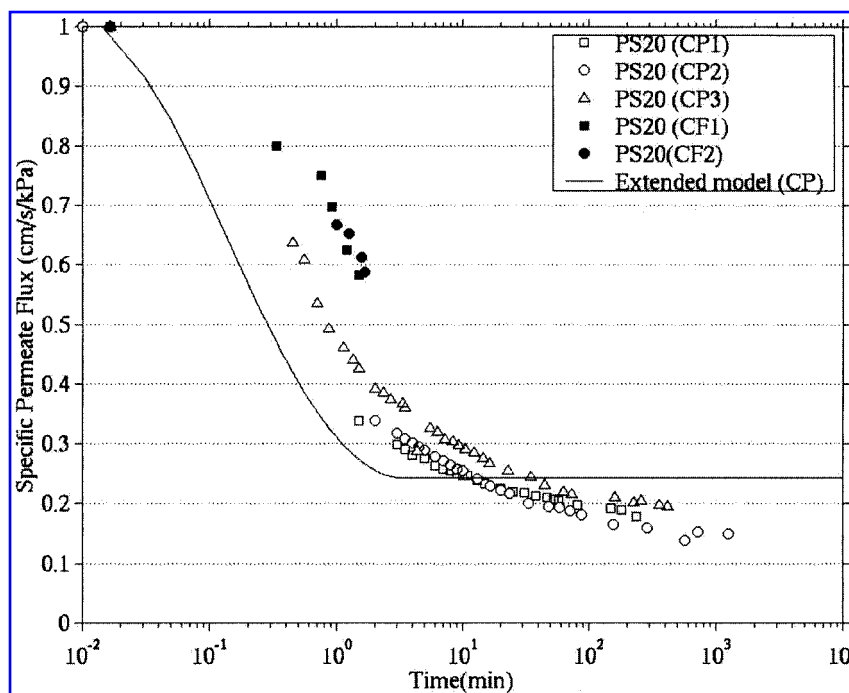
^aCalculated from membrane resistance data given in Table 1.

fouling in experiments with 20-nm particles when compared to those with 100-nm particles. Therefore, the list of particles sizes to be tested was expanded to include 50-nm polystyrene beads. Figures 5–8 summarize the specific permeate flux observed in these experiments.

Effect of particle size

The salient feature of the observed dependencies of permeate flux on time is the dramatic change in fouling behavior in crossing from 20- to 50-nm particles. As can

be seen from Figures 5–8, medium-size particles (50 and 100-nm) foul considerably less than predicted from model calculations. The 20-nm particles produced much more rapid fouling, and did so in a fashion similar to that predicted by theory. Pore plugging can be excluded from consideration as the membrane pore size is considerably smaller than 20 nm. The underprediction of specific permeate flux in the presence of the larger (50 and 100 nm) particles can only be attributed to aspects of cake morphology or particle back-transport that are not accounted for in the extended model.

**Figure 5.** Time dependence of normalized specific permeate flux for 20-nm particles.

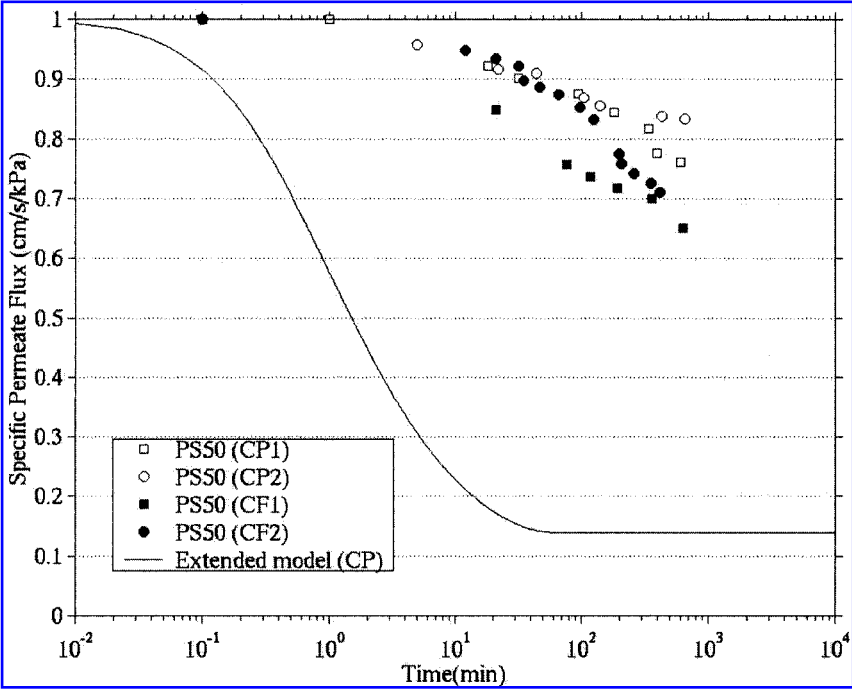


Figure 6. Time dependence of normalized specific permeate flux for 50-nm particles.

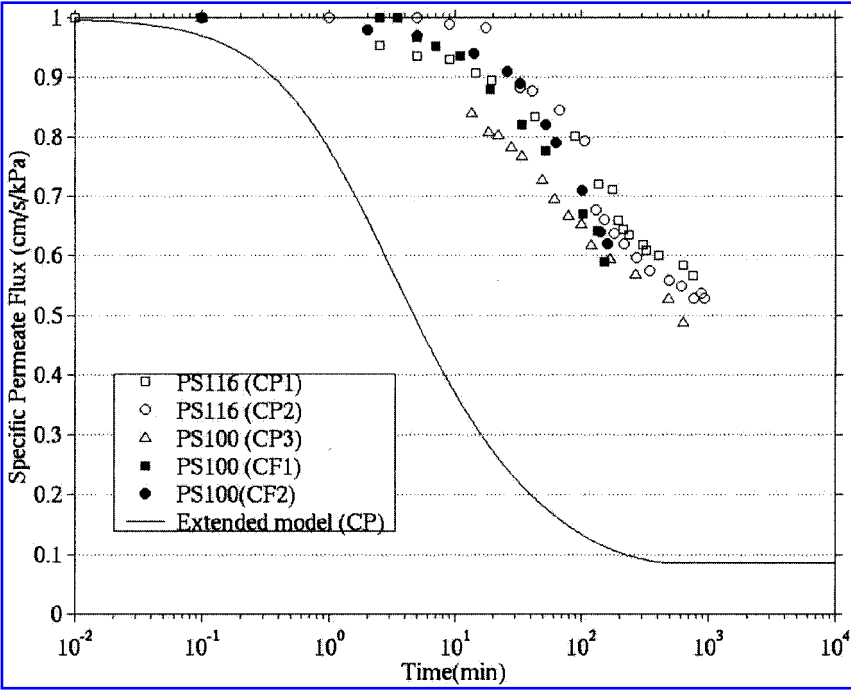


Figure 7. Time dependence of normalized specific permeate flux for 100-nm particles.

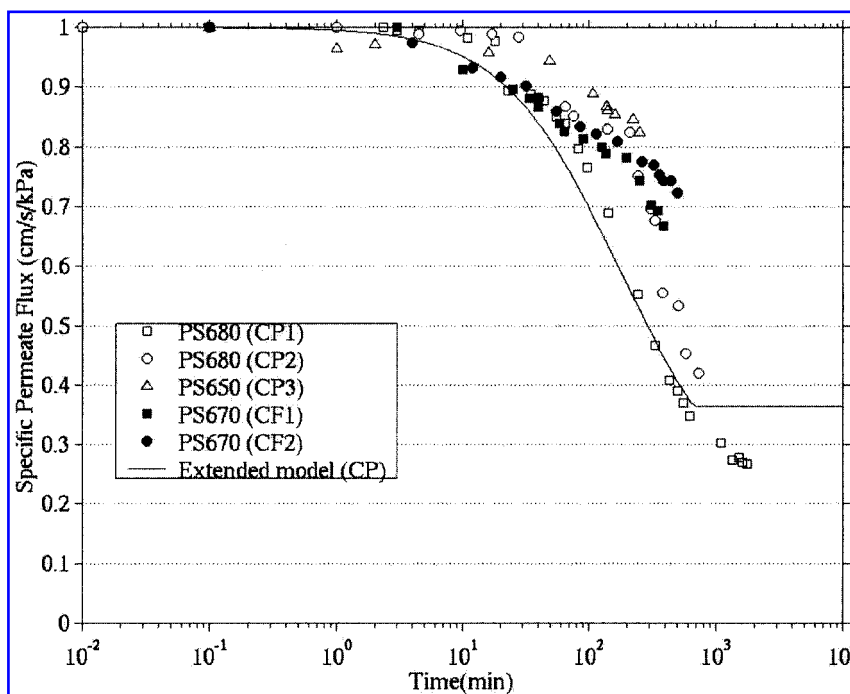


Figure 8. Time dependence of normalized specific permeate flux for 680-nm particles.

Although steady-state flux is grossly underpredicted for 50- and 100-nm particles (Figs. 6 and 7), the experimental permeate flux curves for 20- and 680-nm particles were in general agreement with model predictions (Figs. 5 and 8). Steady-state permeate flux is slightly overpredicted for particles of these smallest and largest sizes.

Effect of operational mode

An important limitation in these experiments was the maximum pressure for the SEPA filtration cell (~690 kPa). This, together with the need to achieve the same initial permeate flux for all experiments, imposed limits on the duration of CF experiments. Even for more permeable membranes, the initial transmembrane pressure needed to provide the target initial flux of 149 L/m²/h was greater than one-half of the maximum 690 kPa pressure, leaving little margin for an increase in the transmembrane pressure in the course of filtration in the CF mode. Consequently, only initial stage of filtration in CF mode was studied.

It should be noted also that in experiments with 20-nm particles, immediately upon the start of experiments, permeate flux dropped quickly. As Fig. 5 illustrates, the flux decreased by the factor of 2 in a matter of 1–2 min, which is approximately the time required to open valves of the setup and for flow meter readings to stabilize. Thus, comparison of CP and CF modes for experiments with 20-nm particles is limited.

For particles of other sizes (50, 100, and 680 nm), differences between the dynamics of specific flux in CF and CP modes are in good qualitative agreement with predictions by the extended model. CP mode is characterized by higher specific fluxes compared with those in CF and these diminish as particle size increases. This result suggests preferential use of CP mode of operation for particles of smaller size.

Modified extended model

The extended model was modified to account for a more complex cake morphology by considering solidosity of the cake to be a function of the distance from the membrane. The dependence was modeled by the following function:

$$\varphi_{c(n)}^{(i)}(x) = \varphi_{\min} + (\varphi_{\max} - \varphi_{\min}) \left[1 + \exp \left(\frac{x - \zeta_{(n)}^{(i)}}{\frac{\Delta_{(n)}}{k}} \right) \right]^{-1} \quad (8)$$

where $\varphi_{\max} = 0.58$, $\varphi_{\min} = \varphi_w$ is the cake solid fraction at the cake-suspension interface that is at the “wall,” x is the distance from the membrane surface: $0 \leq x \leq \delta_{(n)}^{(i)}$, and $\delta_{(n)}^{(i)}$ is cake thickness at the i th grid point and at the n th time step.

The specific cake resistance $R_{c(n)}^{*(i)}$ becomes a function of the cake depth at which it is calculated:

$$R_{c(n)}^{*(i)}(x) = \frac{45\varphi_{c(n)}^{(i)2}(x)}{a_p^2(1 - \varphi_{c(n)}^{(i)}(x))^3} \quad (9)$$

Δ has physical meaning of thickness (in units of particle diameters) of the zone of transition from φ_{\min} to φ_{\max} while ζ corresponds to the distance from the membrane to the location in the cake with solidosity equal to $(\varphi_{\min} + \varphi_{\max})/2$. It can be shown that the choice of $k = 10$ ensures that φ_{\min} value at $\zeta + \Delta/2$ location in the cake is approximated with relative error of less than 0.01. Taking into the account that $\delta_{(n)}^{(i)} = \zeta_{(n)}^{(i)} + \Delta_{(n)}/2$ is the total cake thickness at a given grid point and at a given moment of time, (8) may be rewritten as

$$\varphi_{c(n)}^{(i)}(x) = \varphi_{\min} + (\varphi_{\max} - \varphi_{\min}) \left[1 + \exp \left(\frac{x - \left(\delta_{(n)}^{(i)} - \frac{\Delta_{(n)}}{2} \right)}{\frac{\Delta_{(n)}}{10}} \right) \right]^{-1} \quad (10)$$

It should be noted that the dependence of the thickness of the transition zone Δ on the position along the membrane surface was neglected in this approach. The assumption hinged on the supposition that differences in values of permeate flux corresponding to different positions along the membrane were insufficient to result in differences in Δ values.

Values of δ obtained by solving (6) were used to com-

pute the total cake resistance at each time step n and for each grid point i :

$$R_{c(n)}^{(i)} = \int_0^{\delta_{(n)}^{(i)}} R_{c(n)}^{*(i)} dx. \quad (11)$$

Further, the dimensionless cake resistance:

$$\beta_{(n)}^{(i)} = \frac{H_0}{R_m} \overline{R_{c(n)}^{*(i)}} = \frac{H_0}{R_m} \frac{R_{c(n)}^{(i)}}{\delta_{(n)}^{(i)}}, \quad (12)$$

and dimensionless permeate velocity:

$$v_{w(n)}^{(i)} = \frac{1}{1 + \beta_{(n)}^{(i)} \frac{\delta_{(n)}^{(i)}}{H_0}} = \frac{1}{1 + \beta_{(n)}^{(i)}} \quad (13)$$

were calculated. Numerical values of integrals needed for the computation of g , h , and f functions in (6) were evaluated using routines nag_quad_1d_gen and nag_quad_2d (NAG Fortran 90 Library, release 3).

In an attempt to fit experimental data, a range of Δ (10, 100, 500, and 1,000) and φ_w (0.08, 0.28, 0.38, and 0.48) values were tried as fitting parameters. Although a Δ value of 1,000 in the case of 680-nm particles corresponds to the cake thickness comparable with the channel height and, therefore, is not physical, this value was used in our simulations to illustrate the trend in the permeate flux. The values of φ_w were chosen to cover the range of probable cake porosities. It may be expected that for particles of different sizes, cakes with different porosi-

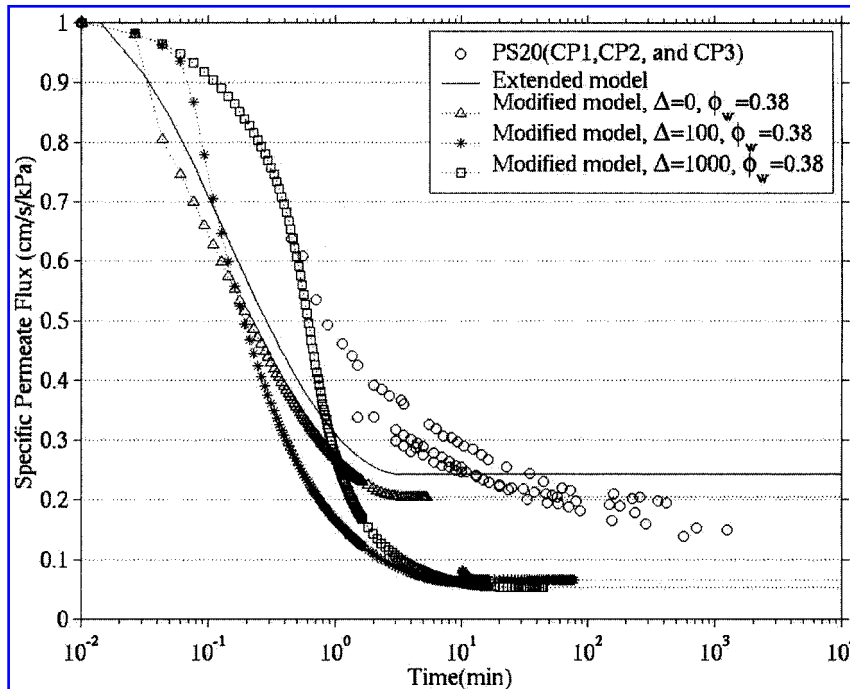


Figure 9. Time dependence of normalized specific permeate flux for 20-nm particles ($\varphi_w = 0.38$, variable Δ).

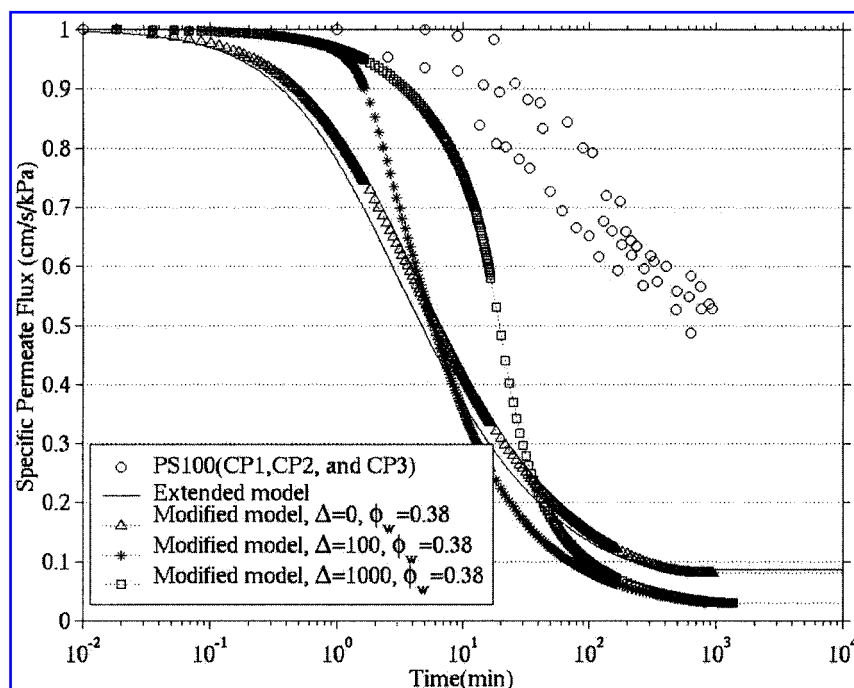


Figure 10. Time dependence of normalized specific permeate flux for 100-nm particles ($\phi_w = 0.38$, variable Δ).

ties at the cake–suspension interface will be formed. In this article, however, we used the same set ϕ_w as a fitting parameter for all cases of different particle sizes looking for a general trend in the permeate flux dependence on ϕ_w . It should also be emphasized that solution

chemistry is known to influence the permeate flux performance in membrane filtration (Faibish *et al.*, 1998). In our experiments, however, both ionic strength and pH were only monitored and were not experimental variables. In the modified extended model, the effect of the

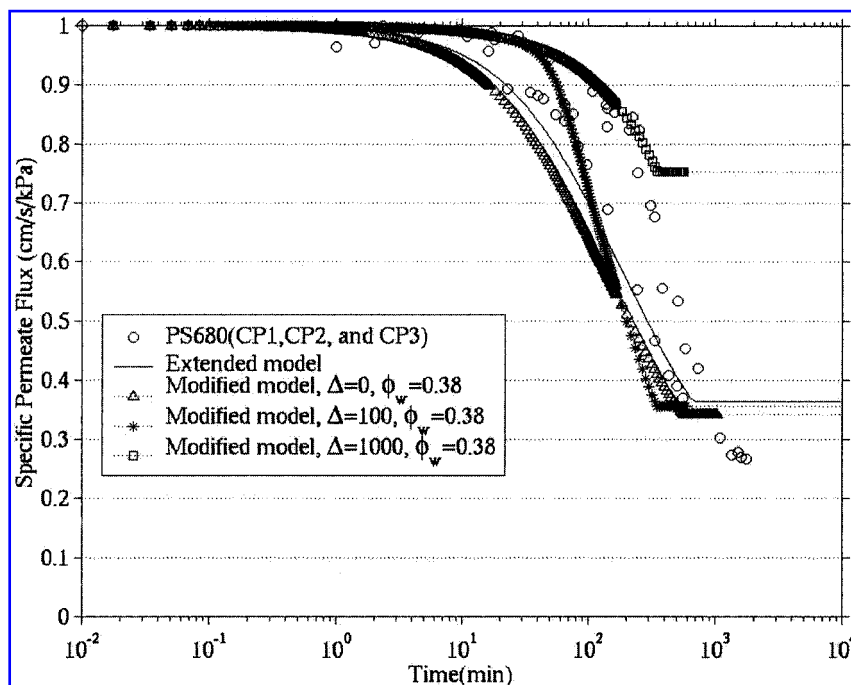


Figure 11. Time dependence of normalized specific permeate flux for 680-nm particles ($\phi_w = 0.38$, variable Δ).

solution chemistry on the cake morphology was not considered.

Some of the simulation results are summarized in Figs. 9–11. No significant improvement in matching modeling and experimental results could be achieved. For example, in the case of 20 nm particles (Fig. 9), using $\varphi_w = 0.38$ allowed for a better match of the steady-state flux but degraded the prediction of the time needed to reach the steady state. A similar tradeoff between the ability to fit the permeate flux and the time to reach the steady state was observed for other particle sizes (Figs. 10 and 11).

The failure to provide a better fit to experimental data using the parametric studies described above implies that the only possible reason for the higher than predicted permeate flux observed in our filtration studies must be that cakes contain fewer particles than the model assumes. It means that additional back-transport mechanisms exist that are not accounted for by the extended model.

Other possible back-transport mechanisms

The extended model assumes a no-slip condition at the cake boundary. If this assumption does not hold and nonzero crossflow at cake–suspension interface exists, it will favor the scouring of intermediate-size particles. This effect would be less for smaller particles because they form cakes with higher resistance and a no-slip condition at the cake boundary may be a reasonable approximation. For bigger particles, a slip velocity would only enhance the tubular pinch effect resulting in a decreased potential for scouring. Another possible factor to take into account is resuspension. This effect may be also at a maximum for the medium-sized particles; big particles have more inertia and are not as easily resuspended while the specific area of interaction of a slipping layer of fluid and the uppermost part of the cake is minimal for small particles, which also decreases their potential for resuspension.

CONCLUSIONS

Permeate flux predictions by the extended model exhibit qualitative agreement with experimentally determined relation between dynamics of permeate flux through membrane filters operated in CP and CF modes. Both modeling and experimental results suggest preferential use of CP mode as particle size decreases. Although the model satisfactorily describes the flux performance in experiments with 20- and 680-nm particles, the fouling behavior for medium-sized particles (50 and 100 nm) differs considerably from theoretical predictions. Simulations involving descriptors of cake morphology as fitting

parameters demonstrated that changes in cake morphology alone cannot account for the observed discrepancies. These results strongly indicate the presence of additional back-transport mechanism(s) leading to cakes containing fewer particles than assumed by the model. Preferential resuspension and scouring of medium-sized particles are hypothesized as such mechanisms.

ACKNOWLEDGMENTS

This work was supported in part by funding through the EPA Hazardous Substances Research Centers/South & Southwest, and in part by the Nanoscience and Engineering Initiative of the National Science Foundation under NSF Award Number EE-0118007.

REFERENCES

- BELFORT, G., DAVIS, R.H., and ZYDNEY, A.L. (1994). The behavior of suspensions and macromolecular solutions in crossflow microfiltration. *J. Membr. Sci.* **96**, 1–58.
- BLATT, W.F., DRAVID, A., MICHAELIS, A.S., and NELSEN, L. (1970). Solute polarization and cake formation in membrane ultrafiltration: Causes, consequences, and control techniques. In: *Membrane Science and Technology. Industrial, Biological, and Waste Treatment Processes*. New York: Plenum Press.
- BOWEN, W.R., and JENNER, F. (1995). Theoretical descriptions of membrane filtration of colloids and fine particles: Assessment and review. *Adv. Colloid Interface Sci.* **56**, 141–200.
- DAVIS, R.H., and LEIGHTON, D.T. (1987). Shear-induced transport of a particle layer along a porous wall. *Chem. Eng. Sci.* **42**(2), 275–281.
- DAVIS, R.H., and SHERWOOD, J.D. (1990). A similarity solution for steady-state crossflow microfiltration. *Chem. Eng. Sci.* **45**, 3204–3209.
- FAIBISH, R.S., ELIMELECH, M., and COHEN, Y. (1998). Effect of interparticle electrostatic double layer interactions on permeate flux decline in crossflow membrane filtration of colloidal suspensions: An experimental investigation. *J. Colloid Interface Sci.* **204**, 77–86.
- GREEN, G., and BELFORT, G. (1980). Fouling of ultrafiltration membranes: Lateral migration and the particle trajectory model. *Desalination* **35**, 129–147.
- LEIGHTON, D., and ACRIVOS, A. (1987). The shear-induced migration of particles in concentrated suspensions. *J. Fluid Mech.* **181**, 415–439.
- LEONARD, E.F., and VASILIEFF, C.S. (1984). The deposition of rejected matter in membrane separation processes. *Chem. Eng. Commun.* **30**, 209–217.

- PORTER, M.C. (1972). Concentration polarization with membrane ultrafiltration. *Ind. Eng. Chem. Prod. Res. Dev.* **11**, 233–248.
- RIPPEGER, S., and ALTMANN, J. (2002). Crossflow microfiltration—State of the art. *Sep. Purif. Technol.* **26**, 19–31.
- ROMERO, C.A., and DAVIS, R.H. (1990). Transient model of crossflow microfiltration. *Chem. Eng. Sci.* **45**(1), 13–25.
- SETHI, S., and WIESNER, M.R. (1997). Modeling of transient permeate flux in cross-flow membrane filtration incorporating multiple particle transport mechanisms. *J. Membr. Sci.* **136**, 191–205.
- STAMATAKIS, K., and TIEN, C. (1993). A simple model of cross-flow filtration based on particle adhesion. *AIChE* **39**(8), 1292–1302.
- STANDARD METHODS FOR THE EXAMINATION OF WATER AND WASTEWATER. (1980). 15th ed. New York: American Public health Association.
- TARABARA, V.V., and WIESNER, M.R. (2002). Computational fluid dynamics simulation of the flow in a laboratory membrane filtration cell operated at low recoveries. *Chem. Eng. Sci.* **58**, 239–246.
- WIESNER, M.R., and CHELLAM, S. (1999). The promise of membrane technology. *Environ. Sci. Technol.* **33**(17), 360A–366A.
- ZYDNEY, A.L., and COLTON, C.K. (1986). A concentration polarization model for the filtrate flux in cross-flow microfiltration of particulate suspensions. *Chem. Eng. Commun.* **47**, 1–21.

This article has been cited by:

1. Marie Dufrechou, Emmanuel Mignard, Michael F. Drenski, Wayne F. Reed. 2014. Filtrodynamics 2: Effects of Particle Size and Filter Type on Trans-Filter Time-Dependent Pressure Signals. *Macromolecular Reaction Engineering* n/a-n/a. [[CrossRef](#)]
2. F.M. Mahdi, R.G. Holdich. 2013. Laboratory cake filtration testing using constant rate. *Chemical Engineering Research and Design* **91**:6, 1145-1154. [[CrossRef](#)]
3. Shankararaman Chellam, N.G. Cogan. 2011. Colloidal and bacterial fouling during constant flux microfiltration: Comparison of classical blocking laws with a unified model combining pore blocking and EPS secretion. *Journal of Membrane Science* . [[CrossRef](#)]
4. Neranga P. Gamage, Shankararaman Chellam. 2011. Aluminum electrocoagulation pretreatment reduces fouling during surface water microfiltration. *Journal of Membrane Science* . [[CrossRef](#)]
5. Anh H. Nguyen, John E. Tobiason, Kerry J. Howe. 2011. Fouling indices for low pressure hollow fiber membrane performance assessment. *Water Research* **45**:8, 2627-2637. [[CrossRef](#)]
6. Jeonghwan Kim, Francis A. DiGiano. 2009. Fouling models for low-pressure membrane systems. *Separation and Purification Technology* **68**:3, 293-304. [[CrossRef](#)]
7. D. Gassara, P. Schmitz, A. Ayadi, M. Prat. 2008. Modelling the Effect of Particle Size in Microfiltration. *Separation Science and Technology* **43**:7, 1754-1770. [[CrossRef](#)]
8. Shankararaman Chellam, Wendong Xu. 2006. Blocking laws analysis of dead-end constant flux microfiltration of compressible cakes. *Journal of Colloid and Interface Science* **301**:1, 248-257. [[CrossRef](#)]
9. J KIM, F DIGIANO. 2006. A two-fiber, bench-scale test of ultrafiltration (UF) for investigation of fouling rate and characteristics. *Journal of Membrane Science* **271**:1-2, 196-204. [[CrossRef](#)]